Journal of Catalysis 407 (2022) 213–220

Contents lists available at ScienceDirect

Journal of Catalysis

journal homepage: www.elsevier.com/locate/jcat

Evidence for redispersion of Ni on $LaMnO_3$ films following high-temperature oxidation

Ohhun Kwon [a,*], Alexandre C. Foucher [b], Renjing Huang [a], Eric A. Stach [b], John M. Vohs [a], Raymond J. Gorte [a,*]

[a] Chemical and Biomolecular Engineering, University of Pennsylvania, Philadelphia, PA 19104, USA
[b] Materials Science and Engineering, University of Pennsylvania, Philadelphia, PA 19104, USA

ARTICLE INFO

Article history:
Received 10 December 2021
Revised 29 January 2022
Accepted 31 January 2022
Available online 07 February 2022

Keywords:
Ni catalyst
Perovskite thin film
Atomic layer deposition
Transmission electron microscopy
Dry reforming of methane

ABSTRACT

$LaMnO_3$ films, 0.5-nm thick, were deposited by atomic layer deposition (ALD) onto γ-Al_2O_3 that had been modified with 15- wt% CaO. The CaO was shown to be effective in preventing formation of $LaAlO_3$ that formed when La_2O_3 was deposited directly onto γ-Al_2O_3. Lattice fringes on the resulting $CaAl_2O_4/\gamma$-Al_2O_3 substrate were weakly resolved, allowing a detailed characterization of the $LaMnO_3$ films. High-resolution transmission electron microscopy (HR-TEM) images showed that the $LaMnO_3$ formed two-dimensional crystallites, ~10–15 nm wide, that covered most of the surface. Crystallites with (001) and (111) orientation were clearly identified. High-temperature oxidation caused Ni to spread over the $LaMnO_3$ film, suggesting there is a reaction of the Ni^{2+} cations with the perovskite lattice. Ni formed by high-temperature reduction on these films remained well dispersed and significantly more active for CO_2 reforming of CH_4 compared to Ni on $MgAl_2O_4$, even after repeated oxidation and reduction cycles at 1073 K. The implications of these results for understanding metal-support interactions between Ni and $LaMnO_3$ are discussed.

Published by Elsevier Inc.

1. Introduction

Perovskite-supported Ni catalysts have received significant attention for high-temperature applications because some perovskites have been shown to stabilize the Ni dispersion and prevent coking [1–3]. For those perovskites that are able to stabilize Ni, the improved sintering characteristics appear to be related to the fact that Ni can become part of the perovskite lattice under oxidizing conditions, subsequently "exsolving" from the lattice to form metal particles under reducing conditions. Although a detailed understanding of how the perovskite prevents coke formation is still lacking, coke tolerance is likely due in part to the fact that the exsolved Ni particles remain partially embedded in the support [4,5]. Finally, it is interesting to notice that the interactions between the metal and the perovskite are perovskite-specific [6,7]. For Ni, this was shown most clearly by the fact that equilibrium constants for Ni oxidation are affected by the perovskite composition [8,9].

There are important problems with using perovskites as the catalyst support, however. First, most perovskites have low surface areas, due in part to the high temperatures required to form the mixed-oxide crystal structure [10,11]. Since the surface area of the metal catalyst cannot be larger than that of the support, the area available for the metal particles dispersed on the perovskite surface is limited. Second, egress-ingress kinetics associated with large perovskite crystallites are too slow to be practical. For large crystallites, it has been shown that the metal particles form within the bulk oxide and are then brought to the surface of the perovskite by strain [5]. And it has been shown that most of the metal remains embedded within the bulk and is therefore inaccessible to gas-phase reactants [12,13]. To circumvent these problems, we have been preparing perovskites as thin films on high-surface-area oxides using atomic layer deposition (ALD). In past work, Ni catalysts were prepared with thin films of $CaTiO_3$ [8], $SrTiO_3$ [8], $BaTiO_3$ [8], $LaFeO_3$ [9], and $LaMnO_3$ [14], all supported on $MgAl_2O_4$. $MgAl_2O_4$ was chosen as the substrate for these studies because it maintains its surface area upon exposure to high temperatures; and, being a compound oxide, $MgAl_2O_4$ is relatively unreactive with the elements that make up many of the perovskites. For example, Al_2O_3 is known to react with La to form $LaAlO_3$, while $MgAl_2O_4$ is at least somewhat resistant to reaction. While SiO_2 is also relatively unreactive, at least one mixed oxide with the perovskite composition was found to be X-ray amorphous on this support [15].

Among the perovskite films that were studied, $LaMnO_3/MgAl_2O_4$ was particularly interesting because Ni on this support showed high reaction rates for CO_2 reforming of CH_4 (e.g. dry reforming of

* Corresponding authors.
E-mail addresses: ohhun@seas.upenn.edu (O. Kwon), gorte@seas.upenn.edu (R.J. Gorte).

https://doi.org/10.1016/j.jcat.2022.01.036
0021-9517/Published by Elsevier Inc.

methane (DRM)), along with excellent thermal stability and coking resistance compared to Ni on $MgAl_2O_4$ [14]. Unfortunately, the crystallinity of the $MgAl_2O_4$ spinel interfered with the study of the perovskite film structure and the interactions of Ni with that perovskite film. To better understand the properties of the $LaMnO_3$ film and the nature of Ni-$LaMnO_3$ interactions, the present work studied $LaMnO_3$ films on $CaAl_2O_4/\gamma$-Al_2O_3. The $CaAl_2O_4/\gamma$-Al_2O_3 support had a lower crystallinity compared to $MgAl_2O_4$ and was also unreactive with La_2O_3, allowing a more detailed study of the perovskite film by transmission electron microscopy (TEM). The results here demonstrate that the $LaMnO_3$ forms two-dimensional crystals with different orientations over the entire substrate. Ni particles supported on these crystallites remain well dispersed and catalytically active following high-temperature treatments.

2. Experimental methods

2.1. Sample preparation

ALD was performed in a homebuilt, static system using procedures that have been described in detail elsewhere [16]. The precursors for CaO, La_2O_3, MnO_x, and NiO were $Ca(TMHD)_2$, $La(TMHD)_3$, $Mn(TMHD)_3$, and $Ni(TMHD)_2$ (TMHD = 2,2,6,6-tetramethyl-3,5-heptanedionato; all precursors were purchased from Strem Chemicals, Inc., USA.). Briefly, the evacuated substrate was exposed for 10 min to a few Torr of the precursor of interest at a temperature of 573 K for $Ca(TMHD)_2$ and 533 K for $La(TMHD)_3$, $Mn(TMHD)_3$, and $Ni(TMHD)_2$. After exposure to one of the precursors, the sample was evacuated, removed from the system, and then calcined in a muffle furnace for 10 min at 873 K to remove the TMHD ligands. One ALD cycle consisted of exposure to the precursor, evacuation, and calcination. The samples were calcined in air using a muffle furnace. Although this ALD protocol differs from that used conventionally, the long precursor-exposure times avoid diffusion limitations and ligand removal at higher temperatures allowed the use of less reactive precursors. That the surface reactions were self-limiting was demonstrated by the linear growth rates. Growth rates for each of the precursors, determined by measuring changes in the sample mass and confirmed by measuring the sample composition using inductively coupled plasma-optical emission spectrometry (ICP-OES), were found to be 7.9×10^{13} Ca/cm^2-cycle, 3.5×10^{13} La/cm^2-cycle, 3.9×10^{13} Mn/cm^2-cycle, and 5.9×10^{13} Ni/cm^2-cycle. The La:Mn ratios for the ALD prepared samples were verified to be around 0.95:1.

The $MgAl_2O_4$ was synthesized in our laboratory by co-precipitation of magnesium nitrate hexahydrate (Sigma-Aldrich, USA) and aluminum nitrate nonahydrate (Sigma-Aldrich, USA) using procedures that are described in detail elsewhere [14]. After calcination to 1173 K for 12 h, the BET surface area of the $MgAl_2O_4$ was 120 m^2/g. The γ-Al_2O_3 was purchased from Strem Chemicals, Inc. (Newburyport, MA, USA, 180 m^2/g) and was also calcined to 1173 K for 12 h prior to use, after which it had a surface area of 100 m^2/g. For samples referred to as $CaAl_2O_4/\gamma$-Al_2O_3, the γ-Al_2O_3 was modified by adding 20 ALD cycles of CaO, resulting in a CaO loading of 15- wt%, to prevent reaction with La_2O_3. This sample had a BET surface area of 63 m^2/g.

The $LaMnO_3$ films were deposited by alternating La and Mn cycles. To achieve the correct La:Mn stoichiometry, we used 19 cycles of Mn and 21 cycles of La. The final loadings of $LaMnO_3$ on $CaAl_2O_4/\gamma$-Al_2O_3 and $MgAl_2O_4$ were 18.6- wt% and 30.6- wt%, respectively, with the higher loading on $MgAl_2O_4$ being due to its higher surface area. Assuming the $LaMnO_3$ formed uniform films with the bulk density of the perovskite, the film thickness on both substrates would be 0.5 nm. Ni was added to $LaMnO_3/CaAl_2O_4/\gamma$-Al_2O_3 using 7 ALD cycles and to $LaMnO_3/MgAl_2O_4$ films using 5 ALD cycles, respectively, resulting in Ni loadings of 5.1 wt% on $LaMnO_3/CaAl_2O_4/\gamma$-Al_2O_3 and 4.3 wt% on $LaMnO_3/MgAl_2O_4$. For reaction measurements, we also compared rates for Ni on other perovskite films on $MgAl_2O_4$; the preparation procedures used for those catalysts were similar to those described above and are described in more detail elsewhere [8]. A list of the samples for which rates were measured, together with some of their key properties, is given in Table 1.

2.2. Characterization methods

The sample crystal structures were probed by X-ray diffraction (XRD) using a Rigaku MiniFlex diffractometer equipped with a Cu Kα source (λ = 0.15416 nm). The sample elemental compositions were determined by ICP-OES performed on a Spectro Genesis spectrometer with a concentric nebulizer, using samples dissolved in Aqua Regia and diluted in a 10- wt% HNO_3 solution [17]. Surface areas were determined from BET isotherms with N_2 adsorption at 78 K using home-built equipment [9]. The range of pressures was between 0 and 60 Torr to linearize the data. We obtained at least 5 points to determine the BET surface area. TEM and scanning transmission electron microscopy (STEM), together with energy dispersive X-ray spectra (EDS), were performed with a JEOL JEM-F200 at an accelerating voltage of 200 kV. STEM images with high magnification and atomic resolution were obtained on a spherical aberration probe corrected JEOL NEOARM 30–200 kV. For STEM imaging, probe size 7 was used with a 40 μm condenser aperture, leading to ~60 pA probe current. Temperature programmed desorption-thermogravimetric analysis (TPD-TGA) measurements were conducted in high vacuum (10^{-7} Torr) in a system equipped with a quadrupole mass spectrometer (RGA100, Stanford Research Systems, Sunnyvale, CA, USA) for product detection and a CAHN 2000 microbalance (Cahn Scientific, Irvine, CA, USA) for determining mass changes. For these measurements, 30-mg samples were saturated with the 10 Torr of 2-propanol (99.9%, Fisher Chemical, Hampton, NH, USA). After 1-h evacuation, TPD-TGA curves were monitored while heating the samples at 10 K min^{-1} to 823 K.

Rates for DRM were measured in a 0.25-in., quartz, tubular flow reactor at atmospheric pressure using 0.1-g samples. Prior to reaction, the samples were calcined in air at 1073 K for 1 h, then reduced in dry H_2 at 1073 K for 1 h. The oxidation and reduction cycles were repeated five times to simulate aging of the catalyst, with reduction being the final step. The products from the reaction were detected with an on-line gas chromatograph (GC, SRI8610C) equipped with a Hayesep Q column and a thermal conductivity detector (TCD). The total flow rate in the reactor was fixed at 110 mL/min, while adjusting the partial pressures by changing the flow rates of CH_4, CO_2, and He. All experiments were conducted after confirming zero conversion in the absence of a catalyst. The conversion was kept below 15% to maintain differential conditions. Each data point was obtained after stabilizing the reaction for 1 h and each point was the average of three measurements. There was no deactivation observed under the conditions of this study.

Table 1
Properties of the samples used for dry reforming of methane.

Catalyst	Specific surface area (m^2/g)	Perovskite loading (wt%)	Ni loading (wt%)
$Ni/MgAl_2O_4$ [8]	115	N/A	4.8
$Ni/CaTiO_3/MgAl_2O_4$ [8]	73	29	4.6
$Ni/SrTiO_3/MgAl_2O_4$ [8]	67	33	3.7
$Ni/BaTiO_3/MgAl_2O_4$ [8]	59	39	4.1
$Ni/LaMnO_3/MgAl_2O_4$	68	28	4.3
$Ni/LaMnO_3/CaAl_2O_4/\gamma$-$Al_2O_3$	41	29	5.1

3. Results

Films with the $LaMnO_3$ stoichiometry were previously formed by ALD on $MgAl_2O_4$ [14]; however, it was not possible to fully characterize the structure of the $LaMnO_3$ film or its influence on the Ni because $MgAl_2O_4$ is highly crystalline, with a spinel structure that has similar lattice parameters to that of the perovskite [18,19]. Therefore, in the present study, $LaMnO_3$ films were studied on a less crystalline $CaAl_2O_4/\gamma\text{-}Al_2O_3$ support. Because La_2O_3 can react with Al_2O_3 to form $LaAlO_3$, the $\gamma\text{-}Al_2O_3$ was first modified by adding 20 ALD cycles of CaO to achieve a loading of 15- wt% CaO. STEM/EDS maps of this sample, reported in Fig. S1, show that the Ca was uniformly distributed over the surface. The uniformity of the CaO was further confirmed by TPD-TGA measurements of adsorbed 2-propanol, shown in Fig. S2. Because $\gamma\text{-}Al_2O_3$ is a Lewis acid, adsorbed 2-propanol undergoes dehydration to propene and water in a sharp feature at ~470 K in TPD [20]. On the $CaAl_2O_4/\gamma\text{-}Al_2O_3$ sample, some 2-propanol desorbs unreacted below 400 K, while the rest reacts to form a mixture of propene and acetone. If the entire $\gamma\text{-}Al_2O_3$ surface had not been completely covered by CaO, a 470-K propene peak should have been observed.

The crystallinity of $CaAl_2O_4/\gamma\text{-}Al_2O_3$ substrates was first analyzed by high resolution-TEM (HR-TEM). A representative HR-TEM image shown in Fig. 1. Although lattice fringes associated with the $CaAl_2O_4$ spinel and $\gamma\text{-}Al_2O_3$ are observed, the fringes from the two phases are difficult to separate and the surface is rough and disordered. The effectiveness of the $CaAl_2O_4$ layer in preventing reaction of La_2O_3 with $\gamma\text{-}Al_2O_3$ is demonstrated in Fig. 2, which shows XRD patterns for the $\gamma\text{-}Al_2O_3$ and $CaAl_2O_4/\gamma\text{-}Al_2O_3$ samples before and after adding La_2O_3 using 15 ALD cycles, followed by calcination at 1073 K for 12 h. The reaction of La_2O_3 with $\gamma\text{-}Al_2O_3$ to form $LaAlO_3$ is clearly observed by the intense peaks associated with a perovskite phase in Fig. 2a. The results for La_2O_3 reaction with $CaAl_2O_4/\gamma\text{-}Al_2O_3$ were dramatically different, as indicated in Fig. 2b. The pattern for $CaAl_2O_4/\gamma\text{-}Al_2O_3$ was distinguished from that of $\gamma\text{-}Al_2O_3$ only by a small peak for a spinel phase at 29 degrees 2θ [21]. After adding La_2O_3 and calcining at 1073 K, the only change was the addition of a small peak at 31 degrees 2θ that corresponds to La_2O_3 [22]. Because diffraction would not be observable for features that have crystallite sizes less than the coherence length of the X-rays (~2 nm) [23], it is possible that the $CaAl_2O_4$ layer simply changes the structure of any $LaAlO_3$ overlayer; however, a simpler explanation is that the $CaAl_2O_4$ forms a barrier that prevents reaction of the La_2O_3 with Al_2O_3.

STEM-EDS data for the $LaMnO_3/CaAl_2O_4/\gamma\text{-}Al_2O_3$ sample are shown in Fig. S3. This sample had 18.6- wt% $LaMnO_3$, corresponding to a 0.5-nm film, and had been calcined to 1073 K for 12 h after the addition of the $LaMnO_3$ film. At this resolution, the STEM image is indistinguishable from that of $\gamma\text{-}Al_2O_3$; but the EDS maps of Ca, La, and Mn show that each of the elements is uniformly distributed over the underlying Al_2O_3. The XRD pattern of the $LaMnO_3/CaAl_2O_4/\gamma\text{-}Al_2O_3$ sample, reported in Fig. 3, exhibits intense peaks associated with a perovskite phase and weak peaks due to $\gamma\text{-}Al_2O_3$. Since La is prevented from reacting with Al_2O_3 by the $CaAl_2O_4$ layer, the perovskite phase must be $LaMnO_3$. Based on the linewidth of the perovskite peaks and the Scherrer Equation, the average crystallite size is estimated to be approximately 12 nm.

To understand the structure of the film, HR-TEM measurements were conducted on the $LaMnO_3/CaAl_2O_4/\gamma\text{-}Al_2O_3$ sample, with two

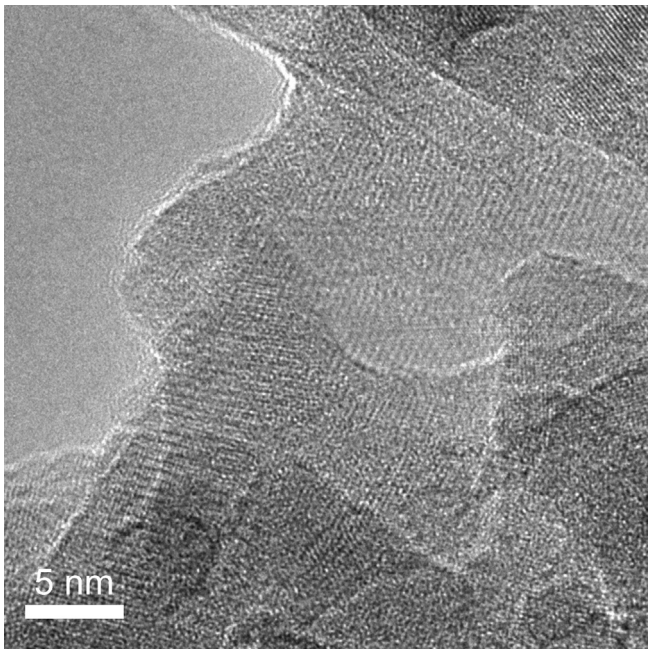

Fig. 1. High resolution (HR)-TEM image of $CaAl_2O_4/\gamma\text{-}Al_2O_3$ sintered at 1073 K for 12 h.

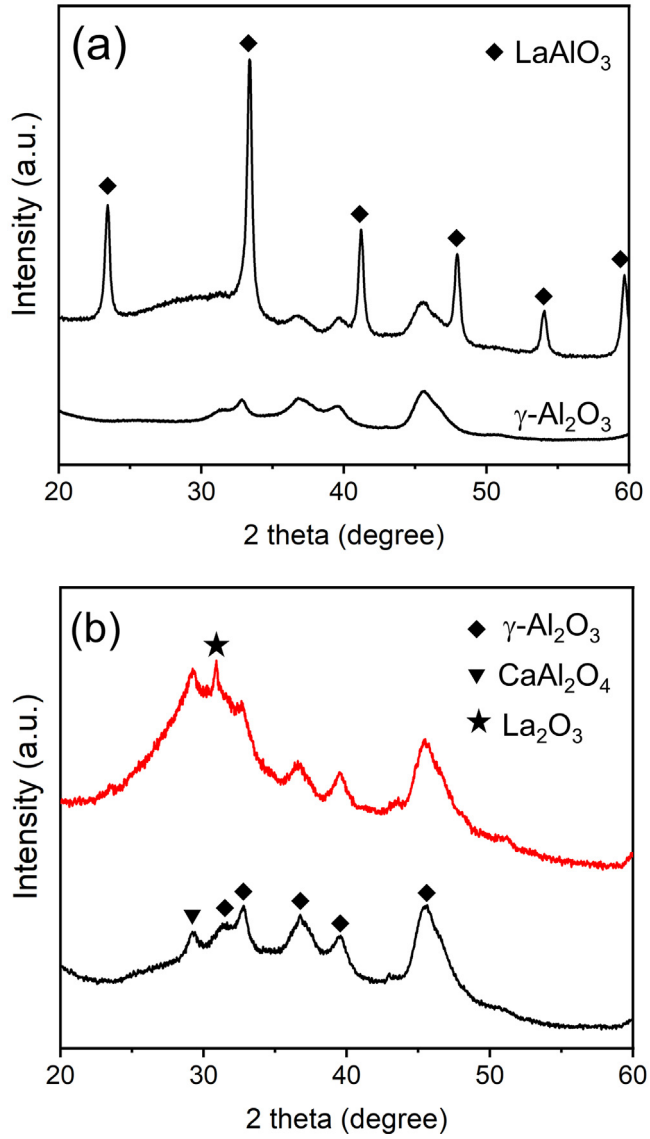

Fig. 2. X-ray diffraction (XRD) patterns for: (a) $\gamma\text{-}Al_2O_3$, before and after adding 15 cycles of La_2O_3 by ALD, followed by calcination to 1073 K for 12 h; (b) $CaAl_2O_4/\gamma\text{-}Al_2O_3$ before and after adding 15 cycles of La_2O_3 by ALD, followed by calcination to 1073 K for 12. Peaks associated with various phases are indicated.

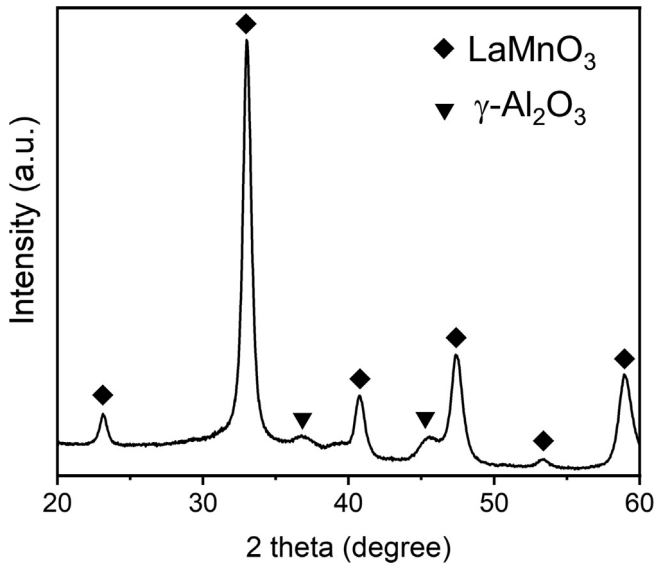

Fig. 3. XRD pattern of the $LaMnO_3/CaAl_2O_4/\gamma\text{-}Al_2O_3$ after calcination at 1073 K for 12 h.

representative images shown in in Fig. 4. The two images indicate the presence of well-define lattice fringes; and the fast Fourier transforms of the images, shown in the upper right-hand corners of each image, indicate that the two crystallites are oriented close to the [0 0 1] and [1 1 1] Zone Axis (Z.A.) orientations, respectively. These crystallites must be two-dimensional since the $LaMnO_3$ loading is only sufficient to form a 0.5-nm film. This conclusion would be valid, even if a significant fraction of the surface were uncovered. If the $LaMnO_3$ crystals in Fig. 4 were three-dimensional cubes, the perovskite loading would be sufficient to cover only about 1% of the surface. X-ray diffraction from these thin films is possible in the direction perpendicular to the surface [23] and a powder pattern is observed in XRD because multiple crystal surfaces are expressed in different parts of the film. Finally, it is worth noting that the lattice spacing for the perovskite phase is the same as that of bulk $LaMnO_3$, within experimental uncertainty. This implies that the density of the film must be similar to that of the bulk perovskite.

To understand how Ni interacts with the $LaMnO_3/CaAl_2O_4/\gamma\text{-}Al_2O_3$ support, 5.1- wt% Ni was added to it by ALD, after which the sample was sequentially oxidized for 1 h at 1073 K and reduced for 1 h at 1073 K, five times. For Ni on bulk $LaMnO_3$ [24], oxidation at this temperature would cause Ni cations to migrate into the perovskite structure, while reduction would exsolve the Ni from the lattice as metal particles. The oxidation–reduction steps were repeated five times since this process has been shown to cause rapid aging by enhancing Ni particle growth in more conventional supported-Ni catalysts [9]. STEM/EDS maps of the oxidized and reduced $Ni/LaMnO_3/CaAl_2O_4/\gamma\text{-}Al_2O_3$ are shown in Fig. 5a and b. The addition of Ni and repeated redox cycles did not have a noticeable effect on the $LaMnO_3$ film morphology, since both La and Mn remain uniformly distributed over the surface. For the oxidized sample, EDS showed the Ni was also uniformly dispersed over the surface, probably indicating that the Ni cations reacted with the film and became part of the perovskite. After reduction, the EDS maps showed that small Ni particles were formed; but some Ni appeared to remain dispersed between the ~2- to 5-nm particles. The fact that the sample had been oxidized and reduced five times prior to these measurements implies that particle formation was reversible, providing additional evidence for the reaction of Ni^{2+} cations with the perovskite film following oxidation. XRD patterns for the oxidized and reduced $Ni/LaMnO_3/CaAl_2O_4/\gamma\text{-}Al_2O_3$, shown in Fig. S4, are similar to that of $LaMnO_3/CaAl_2O_4/\gamma\text{-}Al_2O_3$ in Fig. 3, although there are small, broad peaks at ~37 and 46 degrees 2θ that may be associated with $NiAl_2O_4$. The formation of $NiAl_2O_4$ would imply that some Ni diffused through both the $LaMnO_3$ and the $CaAl_2O_4$ layers to react with the $\gamma\text{-}Al_2O_3$ [25]. There were no peaks in the diffraction pattern that correspond to metallic Ni; but this is to be expected, if metallic Ni is present in particles less than about 2 nm in size.

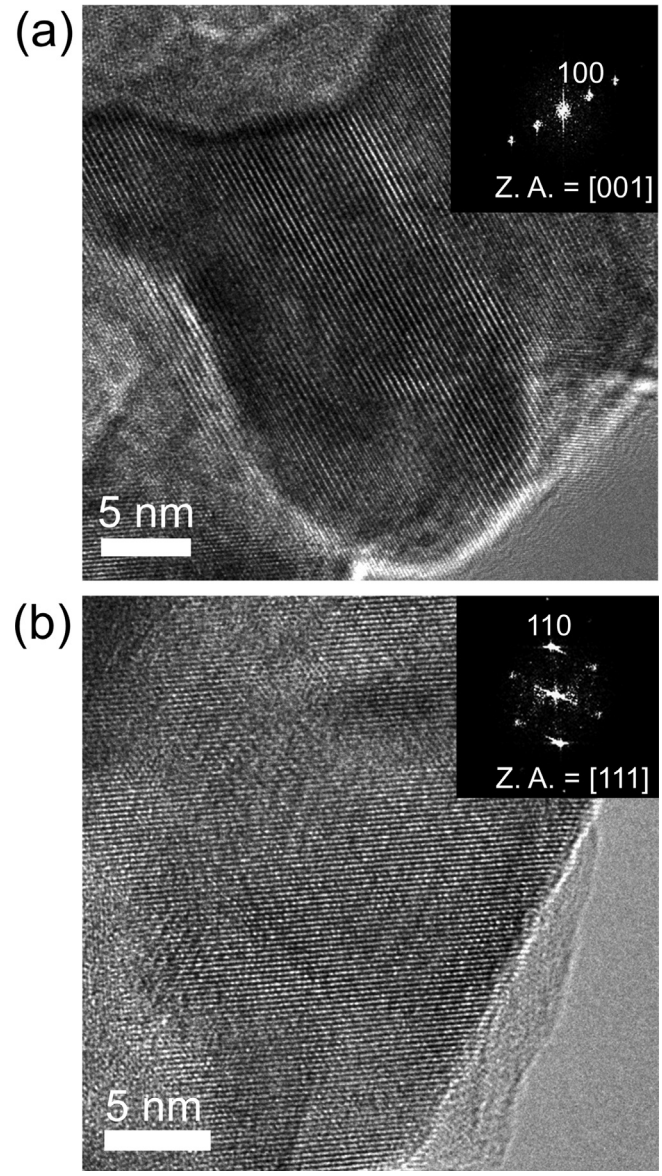

Fig. 4. HR-TEM images and corresponding fast-Fourier transform (FFT) diffractograms of $LaMnO_3/CaAl_2O_4/\gamma\text{-}Al_2O_3$ with (a) Z.A. near [0 0 1] and (b) Z.A. near [1 1 1].

Since only metallic Ni is expected to show activity for DRM, rates for this reaction are useful for determining whether significant amounts of metallic Ni remain are available on a particular catalyst. In catalysts prepared by ex-solution from bulk perovskites, high reduction temperatures are required to bring the metal to the surface [1–3], while reduction of the metal can be accomplished at much lower temperatures on conventional supported metals. Therefore, the effect of reduction temperature on the reaction rates was measured on $Ni/CaAl_2O_4/\gamma\text{-}Al_2O_3$, Ni/

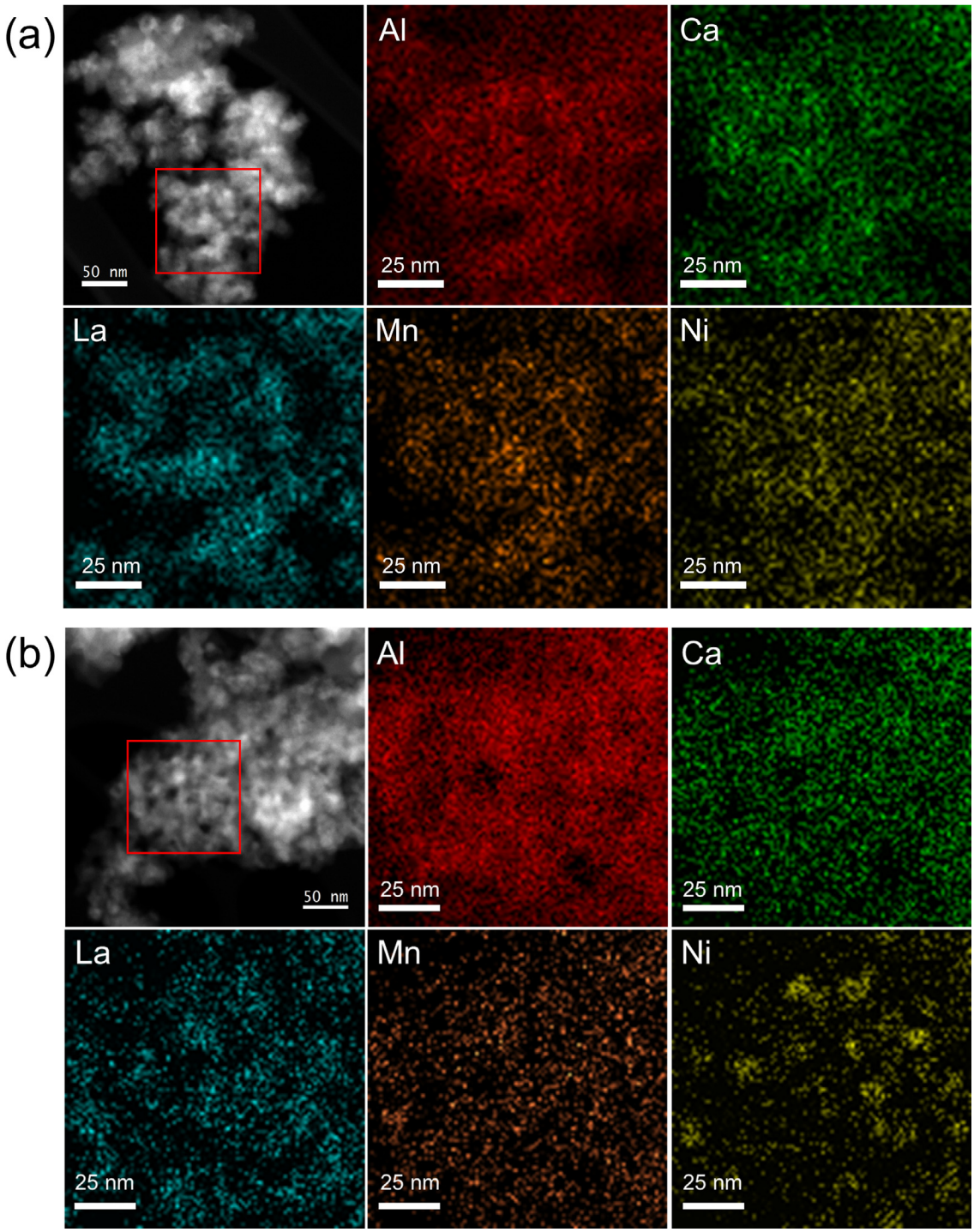

Fig. 5. High-angle annular dark-field (HAADF) STEM images and EDS elemental maps of Al, Ca, La, Mn, and Ni on (a) oxidized and (b) reduced $Ni/LaMnO_3/CaAl_2O_4/\gamma\text{-}Al_2O_3$ after 5 1-h oxidation and reduction cycles at 1073 K.

$LaMnO_3/CaAl_2O_4/\gamma\text{-}Al_2O_3$, and Ni/bulk-$LaMnO_3$. In each case, the catalysts were initially oxidized at 1073 K. As shown in Fig. S5, the activity of the $Ni/CaAl_2O_4/\gamma\text{-}Al_2O_3$ catalyst was essentially the same following reduction at either 773 or 1073 K. By contrast, $Ni/LaMnO_3/CaAl_2O_4/\gamma\text{-}Al_2O_3$ showed a very low activity following reduction at 773 K and became active only after reduction at 1073 K, suggesting that Ni had to be pulled from the perovskite lattice [17]. Although direct comparison of the catalysts prepared from a thin film $LaMnO_3$ to that prepared from bulk $LaMnO_3$ is difficult due to the low surface areas of the bulk perovskite, the data reported in Fig. S5 show a similarity between the bulk and the thin-film $LaMnO_3$-based catalysts in that reduction at 1073 K was required in both catalysts in order to achieve significant rates.

Another difference between conventional Ni catalysts and perovskite-based catalysts is that rates on the perovskite-supported catalysts did not change with repeated redox cycling. The activity for DRM on $Ni/CaTiO_3/MgAl_2O_4$ was the same following the consecutive redox cycles as it was after the first redox cycle, while the activity of $Ni/MgAl_2O_4$ degraded steadily [17]. In the present work, $Ni/LaMnO_3/CaAl_2O_4/\gamma\text{-}Al_2O_3$ exhibited the same activity

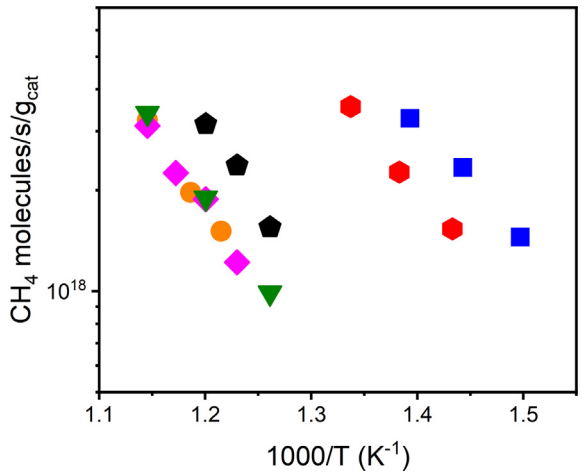

Fig. 6. Steady-state, differential reaction rates for DRM with 35 Torr of CH_4 and CO_2. Rates are shown for Ni/$LaMnO_3$/$CaAl_2O_4$/γ-Al_2O_3 (red hexagon), Ni/$LaMnO_3$/$MgAl_2O_4$ (blue square), Ni/$MgAl_2O_4$ (black pentagon), Ni/$CaTiO_3$/$MgAl_2O_4$ (orange circle), Ni/$SrTiO_3$/$MgAl_2O_4$ (purple diamond), Ni/$BaTiO_3$/$MgAl_2O_4$ (green triangle). Data for the Ti-contain perovskites is reproduced from reference 8. In case of Ni/$LaMnO_3$/$MgAl_2O_4$ and Ni/$LaMnO_3$/$CaAl_2O_4$/γ-Al_2O_3, the samples were oxidized and reduced five times at 1073 K prior to measuring the rates. (For interpretation of the references to colour in this figure legend, the reader is referred to the web version of this article.)

following the first and fifth cycle, as shown in Fig. S6. Finally, DMR rates on Ni/$LaMnO_3$/$MgAl_2O_4$ were essentially independent of CO_2 partial pressure over a wide range, as shown in Fig. S7.

Arrhenius plots of the DRM rates are presented in Fig. 6 for 1073-K reduced Ni/$LaMnO_3$/$CaAl_2O_4$/γ-Al_2O_3 and for the other supported-Ni catalysts listed in Table 1. Each catalyst had a similar Ni loading. Because the Ni/$LaMnO_3$/$CaAl_2O_4$/γ-Al_2O_3 and Ni/$LaMnO_3$/$MgAl_2O_4$ catalysts were roughly an order of magnitude more active than Ni on $MgAl_2O_4$, $CaTiO_3$/$MgAl_2O_4$, $SrTiO_3$/$MgAl_2O_4$, or $BaTiO_3$/$MgAl_2O_4$, rates for these two catalysts were measured at lower temperatures in order to maintain differential conversions under the chosen reaction conditions. It is also noteworthy that rates on Ni/$LaMnO_3$/$CaAl_2O_4$/γ-Al_2O_3 and Ni/$LaMnO_3$/$MgAl_2O_4$ differed by less than a factor of two. Since there was no evidence for $NiAl_2O_4$ formation on Ni/$LaMnO_3$/$MgAl_2O_4$ [14], most of the Ni on Ni/$LaMnO_3$/$CaAl_2O_4$/γ-Al_2O_3 must remain at the surface.

The higher activity of the two $LaMnO_3$-containing catalysts compared to the other catalysts is almost certainly due to better Ni dispersions on these samples. We estimated the Ni dispersion on various perovskites from the particle sizes determined by STEM-EDS analysis, which are included in Fig. S8. This data clearly shows that Ni on $LaMnO_3$ film had a better dispersion compared to $CaTiO_3$, $SrTiO_3$, and $BaTiO_3$. The estimated dispersions and turnover frequencies in Table S1 suggest that specific rates were independent of support, implying support interactions affected only the dispersion.

The interactions between Ni and the $LaMnO_3$/$CaAl_2O_4$/γ-Al_2O_3 support were investigated more carefully using HAADF-STEM imaging on the sample exposed to five oxidation–reduction cycles. As shown in Fig. 7a, oxidized Ni/$LaMnO_3$/$CaAl_2O_4$/γ-Al_2O_3 has clear perovskite lattice fringes but no Ni particles. The EDS elemental map shows that Ni is distributed evenly over the entire surface of the perovskite phase. A representative image of the reduced sample, Fig. 7b, shows a Ni particle on the $LaMnO_3$ crystallite. The particle is roughly 2 nm in size and identifiable both by the lattice fringes, which have a different lattice spacing from that of the perovskite, and by the EDS maps. An image of a slightly larger Ni particle is shown in Fig. S9. This image reveals a Moiré fringe pattern due to the lattice mismatch between Ni and $LaMnO_3$. Because there was no consistent pattern on different Ni particles, the Ni particles are not epitaxially aligned with respect to the underlying perovskite films [26–28]. However, the fact that the Ni particles remain small after high-temperature reduction indicates that there must be interactions with the support that help maintain dispersion.

To confirm that the Ni-$LaMnO_3$ interactions are independent of the support used for the perovskite film, we also re-examined Ni/$LaMnO_3$/$MgAl_2O_4$. The STEM-EDS mapping in Fig. S10 shows that the Ni on the reduced sample was again well dispersed after five oxidation–reduction cycles. Interpretation of the HAADF STEM results on Ni/$LaMnO_3$/$MgAl_2O_4$ is more challenging because of the high crystallinity of $MgAl_2O_4$ but the results are consistent with those observed for Ni on $LaMnO_3$/$CaAl_2O_4$/γ-Al_2O_3. Fig. 8a is a low-magnification image of this sample that shows Ni remains reasonably well dispersed, even after high-temperature redox cycling. Both $LaMnO_3$ and $MgAl_2O_4$ contribute lattice fringes to this image; however, a higher resolution image of a Ni particle on this sample, Fig. 8b, shows a Ni nanoparticle with a lattice spacing of 0.182 nm, corresponding to the (200) planes of metallic Ni metal with the space group of $Fm\bar{3}m$ [2]. The underlying lattice spacing of the support is 0.377 nm, which is consistent with the lattice constant of (100) planes of $LaMnO_3$ with the space group of $Pm\bar{3}m$ [29]. In this particular case, the Ni nanoparticle is aligned with the underlying $LaMnO_3$ lattice, suggesting some bonding interactions between the two phases [30].

4. Discussion

Two important conclusions can be drawn from the present study. First, co-deposition of La_2O_3 and MnO_x onto $CaAl_2O_4$/γ-Al_2O_3 by ALD can result in the formation of relatively large, two-dimensional, perovskite crystals that cover the surface of the support. There does not appear to be any preferred orientation for the crystals, however. Second, Ni particles deposited onto the $LaMnO_3$ films remain highly dispersed and catalytically active following redox treatments at 1073 K.

The formation of two-dimensional perovskite crystals had been inferred previously based on the compositional uniformity of mixed-oxide films and the observation of a diffraction pattern in XRD for films that were thinner than the coherence length of the x-rays [31]. The direct observation of crystallites observed here by HR-TEM confirms the presence of these large crystallites. The fact that the crystallites remain two-dimensional following high-temperature oxidation and reduction treatments indicates that there is likely a thermodynamic driving force to form the crystallites and that there must be attractive interactions between the perovskites and the underlying supports that stabilize the films and prevent formation of three-dimensional particles. Deposition by ALD is likely important only in forming uniform oxide films on the support and for effective mixing of the cations in the initial state. For example, impregnation of supports with metal-salt solutions often results in the formation of particles, rather than films [32]; also, nucleation and growth of oxides from mixed-salt solutions usually results in poor cation mixing at the atomic level. Atomic-scale mixing for synthesis of bulk perovskites at lower temperatures is commonly achieved by the addition of chelating agents, such as citric acid in the Pechini process. There is evidence that the $CaAl_2O_4$/γ-Al_2O_3 and $MgAl_2O_4$ supports act as a template to nucleate growth of the perovskite crystallites, since large crystallites of other perovskites were not observed on silica [15].

The high dispersion observed for Ni on the $LaMnO_3$ crystals, even after high-temperature oxidation–reduction cycling, appears to result from reaction of Ni^{2+} cations with the perovskite under

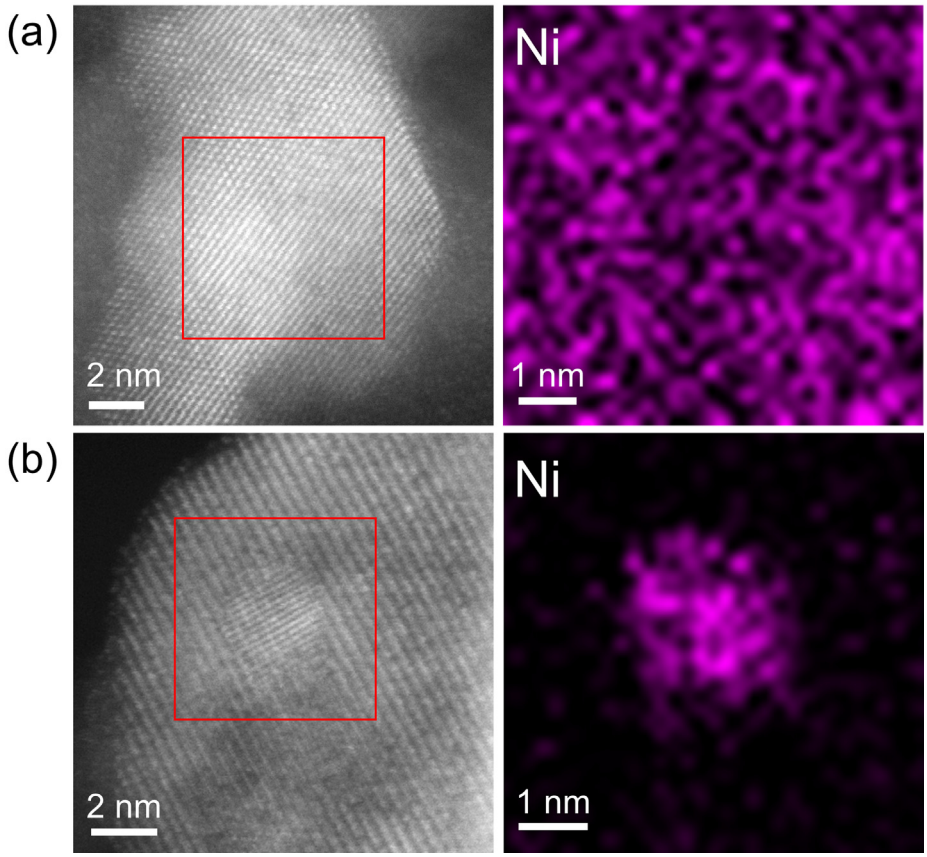

Fig. 7. HAADF STEM images and EDS elemental maps of Ni on (a) oxidized and (b) reduced Ni/$LaMnO_3$/$CaAl_2O_4$/γ-Al_2O_3 after 5 redox cycles at 1073 K.

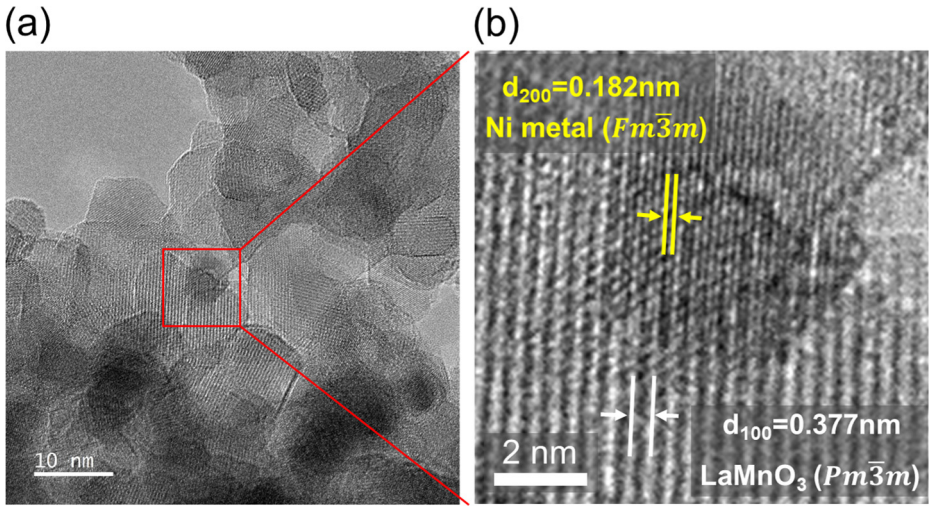

Fig. 8. (a) HR-TEM image and (b) magnified HR-TEM image of reduced Ni/$LaMnO_3$/$MgAl_2O_4$ after 5 redox cycles at 1073 K.

oxidizing conditions. Ni can substitute into the B sites of the $LaMnO_3$ lattice [33], and it is this reversible ingress of Ni cations after high-temperature oxidation and egress of Ni particles upon high-temperature reduction that led to the initial interest in perovskite-supported metals [6,34]. Since the Ni particles formed upon reduction are larger than the thickness of the perovskite films, the concepts developed for ex-solution of metal particles from bulk oxides do not fully apply; however, the bonding interactions between Ni and the perovskite may be similar for the bulk and the thin film perovskites. Unfortunately, we were not able to obtain direct evidence for Ni becoming part of the perovskite lattice. Ni-doped $LaMnO_3$ is still a perovskite structure. Although there should be a change in the lattice parameter upon Ni doping, the lattice parameter also changes oxygen-vacancy concentration [35,36]. While there have been observations of single atoms inside of crystalline lattices, this is accomplished only in highly ideal

cases [37–39]. Interestingly, the bonding interactions are not so strong that the reduced Ni particles become epitaxially aligned with the perovskite, probably because the lattice mismatch is too great.

One of the interesting opportunities that perovskite films present for supported-metal catalysts is the ability to tune the support interactions. Previous studies have shown that the metal-support interactions with perovskites are distinctly different from the interactions of the metal with the individual oxides that make up the perovskite [40]. Also, interactions between a metal and its perovskite support differ with the composition of the perovskite [6]. In the case of Ni, catalysts prepared from $LaFeO_3$ were highly active but underwent deactivation due to oxidation of the Ni at lower temperatures (<873 K) and higher CO_2:CH_4 ratios [9]. $LaMnO_3$-supported Ni catalysts showed higher activity for DRM compared to Ni on $CaTiO_3$, $BaTiO_3$, or $SrTiO_3$ due to better Ni dispersion, suggesting a stronger metal-support interactions. Although it is uncertain how the perovskite supports affect these interactions, one possible reason could be reducibility of the perovskite, since both $LaFeO_3$ and $LaMnO_3$ are more reducible than the titanates.

Predicting which perovskite will provide the optimal properties remains a challenge but recent computational advances show promise for choosing which materials to use. The observation of relatively large crystal facets with (0 0 1) and (1 1 1) orientations is also intriguing. There is evidence from both experimental [12] and computational [41] studies that crystallographic orientation can dramatically affect the interaction with metal particles. With a better understanding of the nucleation and growth of the perovskite crystals, it may be possible to preferentially orient the films. This could provide an additional level of control from the support.

As discussed in the Introduction of this paper, "exsolution" of metal particles from perovskite lattices is an intriguing concept for maintaining the dispersion of metal particles in high-temperature applications. What we have demonstrated here is that the use of perovskite thin films can allow the promise of these catalysts to become a reality. Obviously, there is still much to learn about the nature of these support interactions and the pursuit of this knowledge could result in better heterogeneous catalysts.

5. Conclusions

Thin, ALD-deposited, $LaMnO_3$ films tend to form two-dimensional crystals of varying orientation on $CaAl_2O_4/\gamma\text{-}Al_2O_3$ supports. Reaction of Ni^{2+} cations with the $LaMnO_3$ films under oxidizing conditions allows redispersion of the metal so that the Ni to remains well dispersed, even after repeated oxidation and reduction cycles at 1073 K. Because of the high Ni dispersion, the $LaMnO_3$-supported Ni catalysts exhibit 10-fold higher rates for CO_2 reforming of CH_4 than Ni supported on $MgAl_2O_4$ after similar pretreatments.

Declaration of Competing Interest

The authors declare that they have no known competing financial interests or personal relationships that could have appeared to influence the work reported in this paper.

Acknowledgment

This work was funded by the Department of Energy, Office of Basic Energy Sciences, Chemical Sciences, Geosciences and Biosciences Division, Grant No. DE-FG02-13ER16380. This work was carried out in part at the Singh Center for Nanotechnology, part of the National Nanotechnology Coordinated Infrastructure Program, which is supported by the National Science Foundation grant NNCI-2025608. The authors gratefully acknowledge use of facilities and instrumentation supported by NSF through the University of Pennsylvania Materials Research Science and Engineering Center (MRSEC) (DMR-1720530).

Appendix A. Supplementary material

Supplementary data to this article can be found online at https://doi.org/10.1016/j.jcat.2022.01.036.

References

[1] D. Neagu, G. Tsekouras, D.N. Miller, H. Ménard, J.T.S. Irvine, Nat. Chem. 5 (2013) 916–923.
[2] O. Kwon, S. Sengodan, K. Kim, G. Kim, H.Y. Jeong, J. Shin, Y.-W. Ju, J.W. Han, G. Kim, Nat. Commun. 8 (2017) 15967.
[3] Z. Du, H. Zhao, S. Yi, Q. Xia, Y. Gong, Y. Zhang, X. Cheng, Y. Li, L. Gu, K. Świerczek, ACS Nano 10 (2016) 8660–8669.
[4] D. Neagu, T.-S. Oh, D.N. Miller, H. Ménard, S.M. Bukhari, S.R. Gamble, R.J. Gorte, J.M. Vohs, J.T.S. Irvine, Nat. Commun. 6 (2015) 8120.
[5] T.S. Oh, E.K. Rahani, D. Neagu, J.T.S. Irvine, V.B. Shenoy, R.J. Gorte, J.M. Vohs, J. Phys. Chem. Lett. 6 (2015) 5106–5110.
[6] H. Tanaka, M. Taniguchi, M. Uenishi, N. Kajita, I. Tan, Y. Nishihata, J. Mizuki, K. Narita, M. Kimura, K. Kaneko, Angew. Chem. Int. Ed. 45 (2006) 5998–6002.
[7] C. Lin, A.C. Foucher, Y. Ji, C.D. Curran, E.A. Stach, S. McIntosh, R.J. Gorte, ACS Catal. 9 (2019) 7318–7327.
[8] C. Lin, A.C. Foucher, E.A. Stach, R.J. Gorte, Inorganics 8 (2020) 69.
[9] X. Mao, A.C. Foucher, E.A. Stach, R.J. Gorte, J. Catal. 381 (2020) 561–569.
[10] S. Joo, O. Kwon, K. Kim, S. Kim, H. Kim, J. Shin, H.Y. Jeong, S. Sengodan, J.W. Han, G. Kim, Nat. Commun. 10 (2019) 697.
[11] G. Tsekouras, J.T.S. Irvine, J. Mater. Chem. 21 (2011) 9367–9376.
[12] K.J. Kim, H. Han, T. Defferriere, D. Yoon, S. Na, S.J. Kim, A.M. Dayaghi, J. Son, T.-S. Oh, H.M. Jang, G.M. Choi, J. Am. Chem. Soc. 41 (2019) 7509–7517.
[13] M.B. Katz, S. Zhang, Y. Duan, H. Wang, M. Fang, K. Zhang, B. Li, G.W. Graham, X. Pan, J. Catal. 293 (2012) 145–148.
[14] O. Kwon, R. Huang, T. Cao, J.M. Vohs, R.J. Gorte, Catal. Today 382 (2021) 142–147.
[15] T. Cao, O. Kwon, J.M. Vohs, R.J. Gorte, Int. J. Green Energy (2021) 1–9.
[16] T.M. Onn, R. Küngas, P. Fornasiero, K. Huang, R.J. Gorte, Inorganics 6 (2018) 34.
[17] C. Lin, J.B. Jang, L. Zhang, E.A. Stach, R.J. Gorte, ACS Catal. 8 (2018) 7679–7687.
[18] J. Zhang, T. Lu, X. Chang, N. Wei, J. Qi, Nanoscale Res. Lett. 8 (2013) 261.
[19] J. Du, Z. Yao, S. Han, W. Li, J. Magnes. Alloy. 5 (2017) 181–188.
[20] S. Roy, G. Mpourmpakis, D.-Y. Hong, D.G. Vlachos, A. Bhan, R.J. Gorte, ACS Catal. 2 (2012) 1846–1853.
[21] S. Shiri, M.H. Abbasi, A. Monshi, F. Karimzadeh, Adv. Powder Technol. 25 (2014) 338–341.
[22] H. Kabir, S.H. Nandyala, M.M. Rahman, M.A. Kabir, A. Stamboulis, Appl. Phys. A. 124 (2018) 820.
[23] C.F. Holder, R.E. Schaak, ACS Nano 13 (2019) 7359–7365.
[24] T. Wei, L. Jia, H. Zheng, B. Chi, J. Pu, J. Li, Appl. Catal. A-Gen. 564 (2018) 199–207.
[25] Y. Kathiraser, W. Thitsartarn, K. Sutthiumporn, S. Kawi, J. Phys. Chem. C 117 (2013) 8120–8130.
[26] D. Su, Y. Zhu, Ultramicroscopy 110 (2010) 229–233.
[27] A. Ishizuka, M. Hytch, K. Ishizuka, Microscopy 66 (2017) 217–221.
[28] H. Wen, H. Zhang, Z. Liu, C. Liu, S. Liu, X. Yang, F. Liu, H. Xie, Appl. Phys. Lett. 113 (2018).
[29] P. Sfirloaga, M. Poienar, I. Malaescu, A. Lungu, P. Vlazan, J. Rare Earths 36 (2018) 499–504.
[30] D. Neagu, V. Kyriakou, I.L. Roiban, M. Aouine, C. Tang, A. Caravaca, K. Kousi, I. Schreur-Piet, I.S. Metcalfe, P. Vernoux, M.C.M. Van De Sanden, M.N. Tsampas, ACS Nano 13 (2019) 12996–13005.
[31] X. Mao, A.C. Foucher, T. Montini, E.A. Stach, P. Fornasiero, R.J. Gorte, J. Am. Chem. Soc. 142 (2020) 10373–10382.
[32] T.M. Onn, S. Zhang, L. Arroyo-Ramirez, Y. Xia, C. Wang, X. Pan, G.W. Graham, R. J. Gorte, Appl. Catal. B Environ. 201 (2017) 430–437.
[33] Y.-C. Hou, M.-W. Ding, S.-K. Liu, S.-K. Wu, Y.-C. Lin, RSC Adv. 4 (2014) 5329–5338.
[34] H. Tanaka, I. Tan, M. Uenishi, M. Kimura, K. Dohmae, Top. Catal. 16 (2001) 63–70.
[35] C. Zhang, K. Zeng, C. Wang, X. Liu, G. Wu, Z. Wang, D. Wang, Ceram. int. 46 (2020) 6652–6662.
[36] S. Choi, S. Sengodan, Y.-W. Ju, J. Kim, J. Hyodo, H.Y. Jeong, T. Ishihara, J. Shin, G. Kim, J. Mater. Chem. A. 4 (2016) 1747–1753.
[37] P.M. Voyles, D.A. Muller, J.L. Grazul, P.H. Citrin, H.-J.L. Gossmann, Nature 416 (2002) 826–829.
[38] K. Benthem, A.R. Lupini, Appl. Phys. Lett. 87 (2005).
[39] J. Hwang, J.Y. Zhang, A. D'Alfonso, L.J. Allen, S. Stemmer, Phys. Rev. Lett. 111 (2013).
[40] X. Mao, A.C. Foucher, E.A. Stach, R.J. Gorte, Inorganics 7 (2019) 113.
[41] S. Abhinav, A. Raman, Vojvodic, Chem. Mater. 32 (2020) 9642–9649.